POLITECNICO DI TORINO
Repository ISTITUZIONALE

Modelling coronary flows: impact of differently measured inflow boundary conditions on vessel-specific computational hemodynamic profiles

(Article begins on next page)

20 September 2024

Modelling coronary flows: impact of differently measured inflow boundary conditions on vessel-specific computational hemodynamic profiles

Maurizio Lodi Rizzini[1], Alessandro Candreva[1,2], Claudio Chiastra[1], Emanuele Gallinoro[3], Karol Calò[1], Fabrizio D'Ascenzo[4], Bernard De Bruyne[3], Takuya Mizukami[3], Carlos Collet[3], Diego Gallo[1], Umberto Morbiducci[1]

[1] Polito^{BIO}Med Lab, Department of Mechanical and Aerospace Engineering, Politecnico di Torino, Torino, Italy

[2] Department of Cardiology, Zurich University Hospital, Zurich, Switzerland

[3] Cardiovascular Center Aalst, OLV-Clinic, Aalst, Belgium

[4] Hemodynamic Laboratory, Department of Medical Sciences, University of Turin, Turin, Italy

Address for correspondence:
Prof. Diego Gallo
PoliTo^{BIO}Med Lab, Department of Mechanical and Aerospace Engineering
Politecnico di Torino
Corso Duca degli Abruzzi 24
10129 Turin, Italy
Tel.: +39 011 0906574
E-mail: diego.gallo@polito.it

Abstract

Background and Objectives

The translation of hemodynamic quantities based on wall shear stress (WSS) or intravascular helical flow into clinical biomarkers of coronary atherosclerotic disease is still hampered by the assumptions/idealizations required by the computational fluid dynamics (CFD) simulations of the coronary hemodynamics. In the resulting budget of uncertainty, inflow boundary conditions (BCs) play a primary role. Accordingly, in this study we investigated the impact of the approach adopted for *in vivo* coronary artery blood flow rate assessment on personalized CFD simulations where blood flow rate is used as inflow BC.

Methods

CFD simulations were carried out on coronary angiograms by applying personalized inflow BCs derived from four different techniques assessing in vivo surrogates of flow rate: continuous thermodilution, intravascular Doppler, frame count-based 3D contrast velocity, and diameter-based scaling law. The impact of inflow BCs on coronary hemodynamics was evaluated in terms of WSS- and helicity-based quantities.

Results

As main findings, we report that: (i) coronary flow rate values may differ based on the applied flow derivation technique, as continuous thermodilution provided higher flow rate values than intravascular Doppler and diameter-based scaling law (p=0.0014 and p=0.0023, respectively); (ii) such intrasubject differences in flow rate values lead to different surface-averaged values of WSS magnitude and helical blood flow intensity (p<0.0020) ; (iii) luminal surface areas exposed to low WSS and helical flow topological features showed robustness to the flow rate values.

Conclusions

Although the absence of a clinically applicable gold standard approach prevents a general recommendation for one coronary blood flow rate derivation technique, our findings indicate that the inflow BC may impact computational hemodynamic results, suggesting that a standardization would be desirable to provide comparable results among personalized CFD simulations of the coronary hemodynamics.

Keywords

Computational hemodynamics, coronary artery, inflow boundary conditions, wall shear stress, helical flow, flow rate measurement techniques, uncertainty of cardiovascular models, thermodilution, intravascular Doppler.

Introduction

In the last years, substantial evidence has established the role of local hemodynamics at the blood-endothelium interface in the onset and progression of atherosclerotic plaques [1–6]. In coronary arteries, on one hand specific wall shear stress (WSS) profiles were associated with early atherosclerosis [7–9], plaque vulnerability and risk of myocardial infarction [10,11]. On the other hand, specific intravascular flow features, such as helical flow, were proven to play an atheroprotective role [12,13].

For the accurate estimation of local hemodynamic features, increasingly refined computational models of coronary blood flow have been developed [14,15]. However, their clinical adoption is still hampered by the fact that patient-specific computational fluid dynamics (CFD) simulations, as all model-based strategies, require the inevitable use of assumptions and idealizations [16–20]. These represent sources of uncertainty undermining the credibility, and the clinical applicability as well, of the resulting hemodynamic models. In this regard, a major source of uncertainty is related to the conditions to be prescribed at the inflow boundary [21,22], since intracoronary flow measurement is uncommon in the clinical practice and theoretical assumptions and/or idealizations are thus required for generating boundary conditions (BCs). Invasively, intracoronary flow velocity can be derived from Doppler recordings [23] or from the Thrombolysis In Myocardial Infarction (TIMI) frame count method based on the contrast velocity propagation during angiographic acquisitions [11,24,25]. From velocity, coronary blood flow rate is derived using information on the vessel diameter obtained from imaging [11,23]. Alternatively, anatomy-based laws directly relating flow to the vessel diameter at specific locations have been formulated. These scaling laws have been first based on minimum energy hypothesis [26] while later studies determined empirical power law flow-diameter relationships specifically for coronary arteries [27]. More recently, the introduction of intracoronary continuous thermodilution has allowed the direct

4

measurement of vessel-specific coronary blood flow rate and resistance in absolute terms (i.e. in ml/min and in Wood unit, respectively) [28] at rest as well as in hyperemia [29]. However, application of continuous thermodilution in the clinical routine is for now limited [30].

Alongside its importance as input of reliable patient-specific CFD simulations, from a clinical perspective coronary blood flow rate is a marker of coronary disease as it allows a direct assessment of coronary perfusion, it identifies the presence of flow-limiting epicardial stenosis and is a surrogate of myocardial ischemia [31]. In this sense, it is well established that a depressed coronary perfusion is a hallmark of poor patient outcome at the long term [31]. The clinical relevance of coronary perfusion has inevitably led to the development of several techniques assessing surrogates of flow rate in coronary arteries. Given that each technique uses a different theoretical and/or practical approach for measuring blood flow rate, perfect agreement amongst the different methods should not be expected.

A previous comparison between intravascular Doppler and continuous thermodilution measurements was performed in terms of blood flow rate [28]. Moreover, intravascular Doppler have been compared to a diameter-based scaling law in terms of blood flow rate and the resulting WSS profiles obtained from patient-specific computational hemodynamic models of 8 mildly diseased coronary bifurcations [22]. To date, a comparative analysis on the impact of the most relevant clinically available techniques to derive inflow BCs on computational hemodynamic results is still lacking.

With the final goal of obtaining reliable biomechanical markers of coronary disease from computational hemodynamics, here we compared the effect of deriving inflow BCs from four different *in vivo* techniques assessing clinical surrogates of flow rate on the results of angiography-based CFD simulations.

Methods

The workflow of the study, from image and flow-derived data acquisition to vessel geometry reconstruction, and from CFD to post-processing, is presented in **Figure 1**.
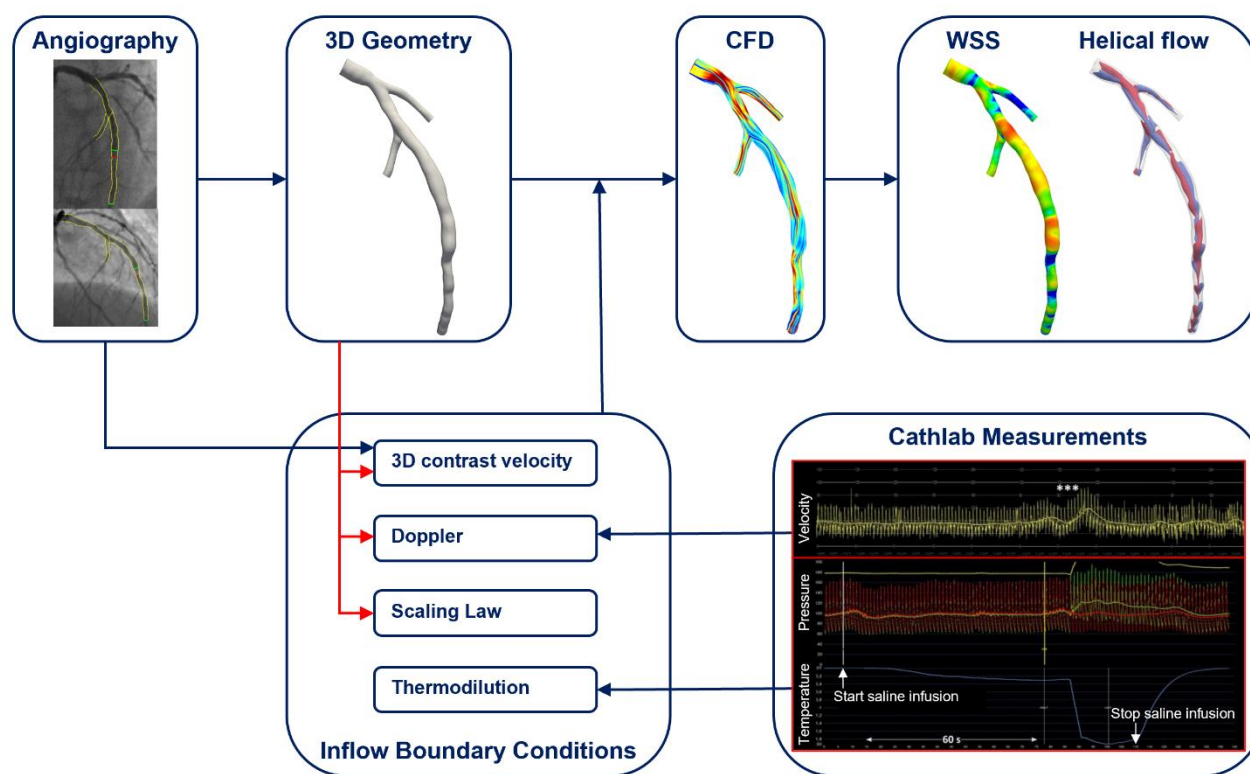

Figure 1. Workflow of the study. Coronary angiography was used to reconstruct 3D models of the coronary arteries and to assess contrast velocity-based flow rate. The diameter-based scaling law for flow rate assessment was applied directly to the 3D reconstructed geometries, while thermodilution and Doppler flow rate measurement were performed in the cathlab. The assessed flow rates were prescribed as inflow boundary conditions to computational fluid dynamics simulations to obtain wall shear stress and intravascular flow data.

Patient selection and 3D vessel reconstruction

Fourteen vessels (7 left anterior descending, LAD, and 7 right coronary arteries, RCA) from 14 patients (92.5% of male gender, mean age 63.2±7.88 years) undergoing clinically indicated coronary angiography and invasive assessment of the coronary microcirculation underwent sequential intracoronary Doppler [23] and continuous thermodilution measurements [32]. The study protocol is exhaustively detailed elsewhere [29]. The study was approved by the Institutional Review Board at Cardiovascular Center Aalst (Aalst,

Belgium) and conformed to the Helsinki Declaration on human research of 1975, as revised in 2000. Informed consent was obtained from the patients.

Invasive flow measurements were performed in vessels with estimated visual diameter stenosis below 30%. 3D coronary reconstructions were performed using two angiographic projections at least 25° apart combining a commercially available software (QAngio XA Bifurcation RE, Medis medical imaging systems, Leiden, The Netherlands) and a custom-made algorithm [33]. Side branches with diameter larger than 1 mm were included [33]. The reconstructed 3D vascular models are presented in **Supplementary Figure 1**.

Coronary flow rate estimation procedures

Coronary blood flow rate was assessed in resting conditions with four different techniques: continuous thermodilution [28,32]; Doppler ultrasound [23]; 3D contrast velocity [11]; diameter-based scaling law [27].

Intracoronary continuous thermodilution was performed using a dedicated infusion microcatheter with 4 lateral side holes (RayFlow™, Hexacath, Paris, France) loaded on the pressure/temperature wire (PressureWire™ X, Abbott Vascular, Santa Clara, CA, USA) and connected to a 200 cc syringe of injector (Medrad® Stellant, Medrad Inc, Warrendale, PA, USA) filled with saline at room temperature (between 21 and 22°C) and placed in the first millimetres of the artery under investigation [30]. Distally, the saline was infused at an infusion rate of 10 mL/min during 60 to 90 seconds and the thermodilution-derived flow rate (Q_{thermo}) was estimated according to the formula [34]:

$$Q_{thermo} = \gamma \, \frac{T_i}{T} Q_i \qquad (1)$$

where Q_i is the infusion rate of saline, T_i is the temperature of the infused saline, T is the temperature of the homogeneous mixture of blood and saline measured in the distal part of coronary artery with the pressure/temperature wire, and the quantity γ=1.08 accounts for

7

the densities and specific heat of blood and saline [30]. Q_{thermo} unit of measure is expressed as mL/min.

Intravascular Doppler flow velocity estimation was performed using a dedicated coronary Doppler velocity wire (FloWire®, Philips/Volcano, San Diego, CA, USA) connected to a Doppler system (FlowMap®, Cardiometrics; Mountain View, CA, USA) and advanced in the distal part of the artery, at the same location as the pressure/temperature wire. [29]. Time-dependent Doppler signals were acquired using the physiologic tracings recorder (Mac-Lab™ Hemodynamic Recording System, GE Healthcare, Chicago, IL, USA). The cycle-average Doppler flow rate ($Q_{Doppler}$) at the inflow section of each vessel was estimated assuming a parabolic velocity profile [23], according to the formula:

$$Q_{Doppler} = A \cdot \frac{APV}{2} \qquad (2)$$

where A is the area of the inlet surface and APV is the cycle-Average Peak Velocity value from Doppler flow measurements.

The 3D contrast velocity method [11] for determining inlet flow rate is based on the number of angiographic frames required for contrast to travel from the vessel ostium to a standardized distal coronary landmark. In detail, using the number of frames (N) visually counted by an expert operator and the distance (L) of the coronary landmark from the ostium as computed on the 3D anatomical reconstruction of the vessel, the average flow rate (Q_{CV}) can be estimated according to the formula:

$$Q_{CV} = A \cdot \frac{L \cdot f}{N} \qquad (3)$$

where f is the frame rate of acquisition of the angiographic images.

The average coronary flow rate (Q_{SL}) was also estimated according to the anatomy-based scaling law:

8

$$Q_{SL} = \alpha \cdot d^{\beta} \qquad\qquad (4)$$

where the volumetric flow rate Q_{SL} was expressed in m^3/s by van der Giessen et al. [27], being d the hydraulic diameter of the inflow section measured in m and the values of the parameters $\alpha = 1.43\ m^{0.45}/s$ and $\beta = 2.55$ [27].

Computational fluid dynamics simulations

For each 3D coronary artery model, four steady-state CFD simulations were carried out, each of them testing one of the four estimated flow rate values as inflow boundary condition. A total of 56 steady-state CFD simulations was carried out. The estimated average flow rates were prescribed in terms of parabolic velocity profile at the inflow section of the fluid domain, as suggested by previous studies [33]. The fluid domain was discretized combining tetrahedral elements with 5 near-wall prismatic layers using the software ICEM CFD (Ansys Inc., Canonsburg, PA, USA) and adopting meshing parameters derived from a grid independence analysis performed in a previous study [12]. The discretized governing equations of fluid motion, the Navier-Stokes equations, were then solved using the finite volume-based code Fluent (Ansys Inc.). Blood was assumed as a homogeneous and incompressible fluid (density $\rho=1060\ kg/m^3$), and its non-Newtonian behaviour was modelled using the Carreau model ($\mu_\infty=0.0035$ Pa·s, $\mu_0=0.25$ Pa·s, $\lambda=25$ s, and n=0.25) [35]. The coronary vessel wall was assumed to be rigid with no-slip conditions. The boundary conditions at the outflow were prescribed according to the widely adopted strategy of setting the flow split at each coronary bifurcation according to a diameter-based scaling law [27]. Details on the adopted numerical schemes are reported in the **Supplementary Materials**.

The impact of the adopted flow rate as inflow BC on CFD simulations was evaluated in terms of WSS distribution at the luminal surface and intravascular flow features. The flow rate from

9

continuous thermodilution was assumed as reference since this technique provides a direct measurement of absolute flow rate, according to eq. (1).

Wall shear stress

The luminal distribution of the WSS magnitude and the absolute error in WSS direction (AEWSSD) were analysed: the former quantifies the local magnitude of the fluid shear stress at the blood-endothelium interface; the latter quantifies the inflow BC-dependent local misalignment of the WSS according to the formula [36,37]:

$$\text{AEWSSD} = 1 - \frac{|\mathbf{WSS}_{\text{thermo}} \cdot \mathbf{WSS}_{\text{BC}}|}{|\mathbf{WSS}_{\text{thermo}}| \cdot |\mathbf{WSS}_{\text{BC}}|} \qquad (5)$$

where $\mathbf{WSS}_{\text{thermo}}$ is the local WSS vector obtained when the reference flow rate Q_{thermo} is prescribed as inflow BC, and $\mathbf{WSS}_{\text{BC}}$ is the WSS vector field obtained when Q_{Doppler}, Q_{CV} or Q_{SL} are prescribed. AEWSSD ranges from 0, indicating a perfect alignment between vectors, to 1, corresponding to an angle of ±90° between the vectors. The impact of the inflow BC on WSS magnitude was also quantified in terms of luminal surface area exposed to low WSS, an indicator of hemodynamic risk in the early stages of the atherosclerotic process [7–9]. Technically, on each vessel the low WSS surface area was assessed by calculating the percentage of luminal surface exposed to WSS magnitude values below the 10$^{\text{th}}$ percentile (WSS10) [12,38] of the WSS magnitude distribution obtained pooling together data from the four simulations carried out over each vessel. On each vessel, the co-localization of WSS10 surface areas from Q_{Doppler}-based, Q_{CV}-based and Q_{SL}-based simulations with the Q_{thermo}-based one was assessed by applying the Jaccard similarity index (SI) [39]:

$$\text{SI} = \frac{2(\text{WSS10}_{\text{thermo}} \cap \text{WSS10}_{\text{BC}})}{\text{WSS10}_{\text{thermo}} \cup \text{WSS10}_{\text{BC}}} \qquad (6)$$

where WSS10$_{\text{thermo}}$ is the luminal surface area exposed to low WSS magnitude when Q_{thermo} is prescribed as inflow BC and WSS10$_{\text{BC}}$ is the luminal surface area exposed to low WSS

10

magnitude when $Q_{Doppler}$, Q_{CV} or Q_{SL} are prescribed. The SI of eq. (6) ranges from 0 (no co-localization) to 1 (perfect co-localization). The inflow rate-dependent local WSS misalignment with respect to **WSS**thermo was evaluated comparing probability density functions and the luminal surface AEWSSD profiles.

Based on theory, WSS magnitude in arteries can be markedly affected by the absolute flow rate value. As perfect agreement amongst the different methods for measuring blood flow rate should not be expected, here normalized WSS magnitude (normWSS) was also analysed. Normalized WSS was obtained by dividing the local absolute WSS magnitude values by WSS magnitude value as obtained applying the Hagen-Poiseuille theory at the inflow section of the model geometry (with dynamic viscosity derived from the adopted Carreau model for blood rheology, calculated at the characteristic shear rate corresponding to the inlet average velocity [40,41]. Moreover, to verify if the WSS magnitude profiles obtained from steady-state simulations are representative of the WSS magnitude distribution also under transient-flow conditions, unsteady-state simulations were carried out, as detailed in the **Supplementary Materials**. From the unsteady-state simulations, the distribution of time averaged wall shear stress (TAWSS), a well-established hallmark of coronary artery disease [9,42,43], was analysed and compared to steady-state WSS magnitude profiles.

Intravascular flow

Intravascular coronary flow was investigated in terms of helical flow patterns, which were visualized in terms of local normalized helicity (LNH), a measure quantifying the local alignment between velocity and vorticity vectors according to [44]:

$$\text{LNH} = \frac{\mathbf{v(x) \cdot \boldsymbol{\omega}(x)}}{|\mathbf{v(x)}||\boldsymbol{\omega}(x)|} = \cos \varphi(\mathbf{x}) \qquad (7)$$

11

where $\mathbf{v}$ and $\boldsymbol{\omega}$ are velocity and vorticity vectors, respectively, and φ is the angle between velocity and vorticity vectors. In addition, a quantitative description of helical flow features was provided considering four well-established helicity-based hemodynamic descriptors [38,45], namely the volume-average helicity (h_1), the volume-average helicity intensity (h_2), the signed balance of counter-rotating helical structures (h_3), and the unsigned balance of counter-rotating helical structures (h_4), derived in steady-state form as:

$$h_1 = \frac{1}{V} \int_V \mathbf{v}(\mathbf{x}) \cdot \boldsymbol{\omega}(\mathbf{x}) dV \qquad (8)$$

$$h_2 = \frac{1}{V} \int_V |\mathbf{v}(\mathbf{x}) \cdot \boldsymbol{\omega}(\mathbf{x})| dV \qquad (9)$$

$$h_3 = \frac{h_1}{h_2} \qquad -1 \leq h_3 \leq 1 \qquad (10)$$

$$h_4 = \frac{|h_1|}{h_2} \qquad 0 \leq h_4 \leq 1 \qquad (11)$$

where V is the integration volume of the fluid domain of interest. h_1 represents the average amount of helical flow and h_2 quantifies its intensity, while h_3 and h_4 measure the prevalence (identified by the sign) and the strength of relative rotations of helical flow structures, respectively.

To verify if the helical flow features obtained from steady-state simulations are representative of the average intravascular flow patterns also under transient-flow conditions, unsteady-state simulations were carried out, as detailed in the **Supplementary Materials**. From the unsteady-state simulations, cycle-average values of the helicity-based descriptors [38] were analysed and compared to the steady-state ones of equations (8-11).

Statistical analysis

The Shapiro-Wilk test was applied to verify the normality of data distributions due to the small sample investigated. Parametric coupled t-tests or non-parametric Wilcoxon tests, as

12

appropriate, were used for comparing continuous variable distributions. Continuous thermodilution was assumed as reference measurement procedure. Correlation between measurement procedures was assessed using Pearson or Spearman coefficients, as appropriate, while agreement between measurement procedures with the Bland-Altman method [46]. The significance threshold was set at 0.05. All statistical analyses were performed in Matlab (The MathWorks Inc., Natick, MA, USA).

Results

Coronary blood flow rate estimates

Coronary flow rate estimates and corresponding Reynolds numbers at the inflow section of each vessel are summarized in **Supplementary Table 1**. Continuous thermodilution-derived flow rate values Q_{thermo} (68.20 [52.61-81.81] mL/min) were significantly higher than $Q_{Doppler}$ values (43.99 [32.40-67.62] mL/min; p=0.0014) and Q_{SL} values (34.51 [30.12-43.41] mL/min; p=0.0023) and lower than Q_{CV} (78.25 [57.32-97.24]; p=0.2368), **Figure 2A**. A moderate linear correlation emerged between Q_{thermo} and $Q_{Doppler}$ (r=0.54, 95% CI 0.01 to 0.83, p=0.0473), **Figure 2B**.
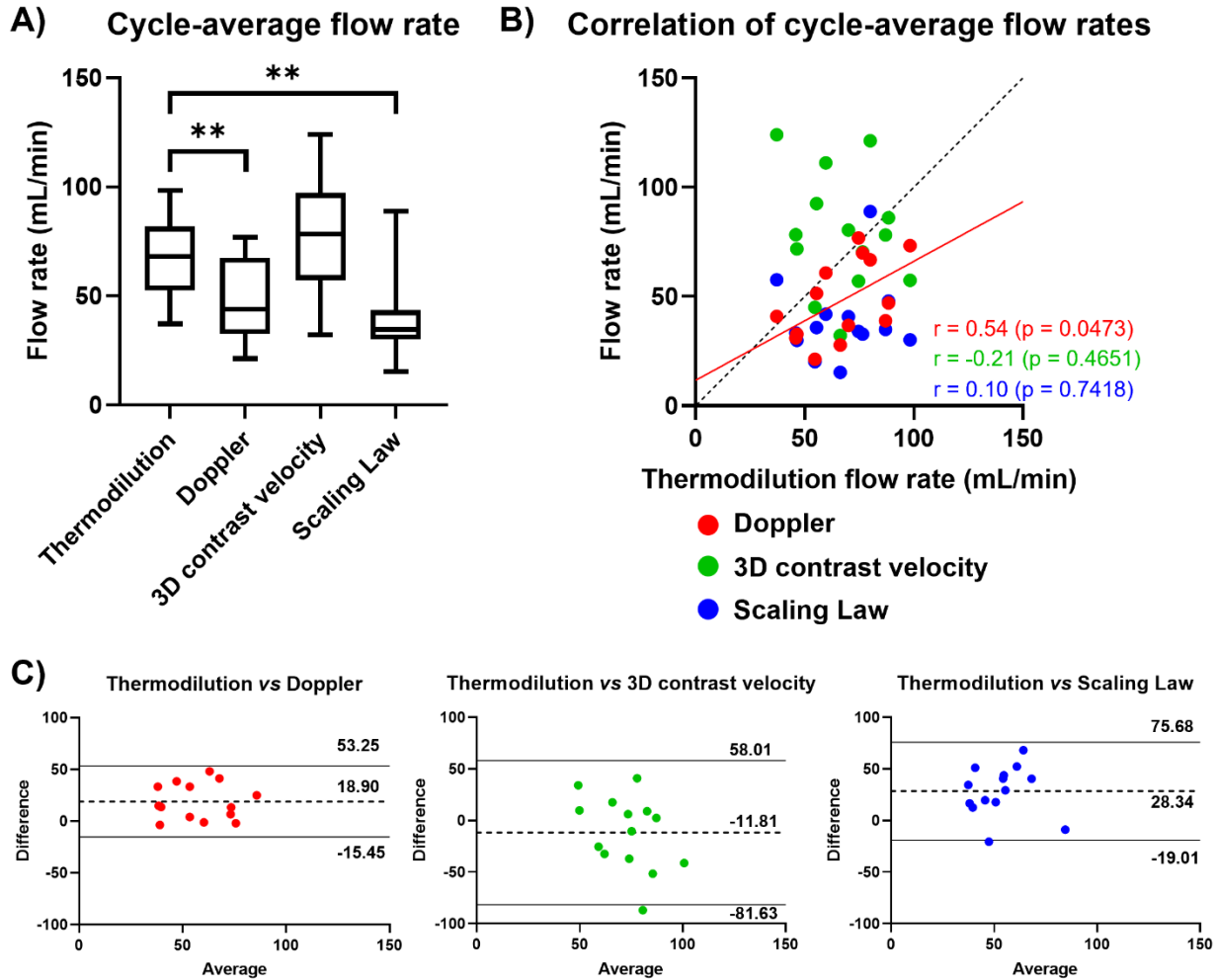
Figure 2. (A) boxplot representation of the assessed cycle-average flow rate distributions per adopted technique. Statistically significant differences, evaluated between thermodilution and the other flow rate assessment techniques, are indicated with ** ($p<0.01$); (B) scatter plot of thermodilution-based vs. Doppler-based, 3D contrast velocity-based and scaling law-based flow rate assessment. Linear regression line was reported only for Doppler-based flow rate due to the emerged significant linear correlation (as reported in figure). The black dotted line represents the identity line; (C) Bland-Altmann plots of Doppler-based, 3D contrast velocity-based and scaling law-based vs. thermodilution-based flow rate values.

Results from the Bland-Altman analysis are presented in **Figure 2C**. Both scaling law- and Doppler-based procedures lead to an underestimation of the coronary blood flow measured with thermodilution (Q_{thermo} *vs.* $Q_{Doppler}$ bias = 18.90 mL/min; Q_{thermo} *vs.* Q_{SL} bias = 28.34 mL/min), while an opposite trend emerged for 3D contrast velocity method (Q_{thermo} *vs.* Q_{CV} bias = -11.81 mL/min). The lowest data dispersion was found for Q_{thermo} *vs.* $Q_{Doppler}$ (SD = 17.52 mL/min). No significant linear trend in terms of error was observed for $Q_{Doppler}$, Q_{CV}, and Q_{SL} *vs.* Q_{thermo}

14

Impact of flow rate estimation on coronary WSS

WSS magnitude distributions with the four different inflow BCs for the 14 coronary artery models are visually presented in **Supplementary Figure 2**. Two explanatory coronary artery models (one RCA and one LAD) reflecting results common to all the 14 cases are displayed in **Figure 3,** where the WSS magnitude distribution at the luminal surface obtained prescribing Q_{thermo} is presented with the local percentage differences (absolute values) from it in terms of WSS magnitude, obtained when $Q_{Doppler}$, Q_{CV}, and Q_{SL} values are prescribed as inflow BC. A significant difference in terms of luminal surface-averaged values of WSS magnitude emerged between simulations based on Q_{thermo} and $Q_{Doppler}$ as inflow BC (1.69 [1.23-2.30] Pa and 1.05 [0.80-1.76] Pa, respectively; p=0.0020) and simulations based on Q_{thermo} and Q_{SL} (0.80 [0.70-1.40] Pa; p=0.0008) as inflow BC (**Figure 4A**). A significant linear correlation (r=0.65, 95% CI 0.18 to 0.88; p=0.0119) emerged between surface-averaged WSS magnitude median values derived from Q_{thermo} and $Q_{Doppler}$ simulations (**Figure 4B**), in accordance with the emerged correlation between thermodilution and Doppler flow rate measurements (**Figure 2B**).
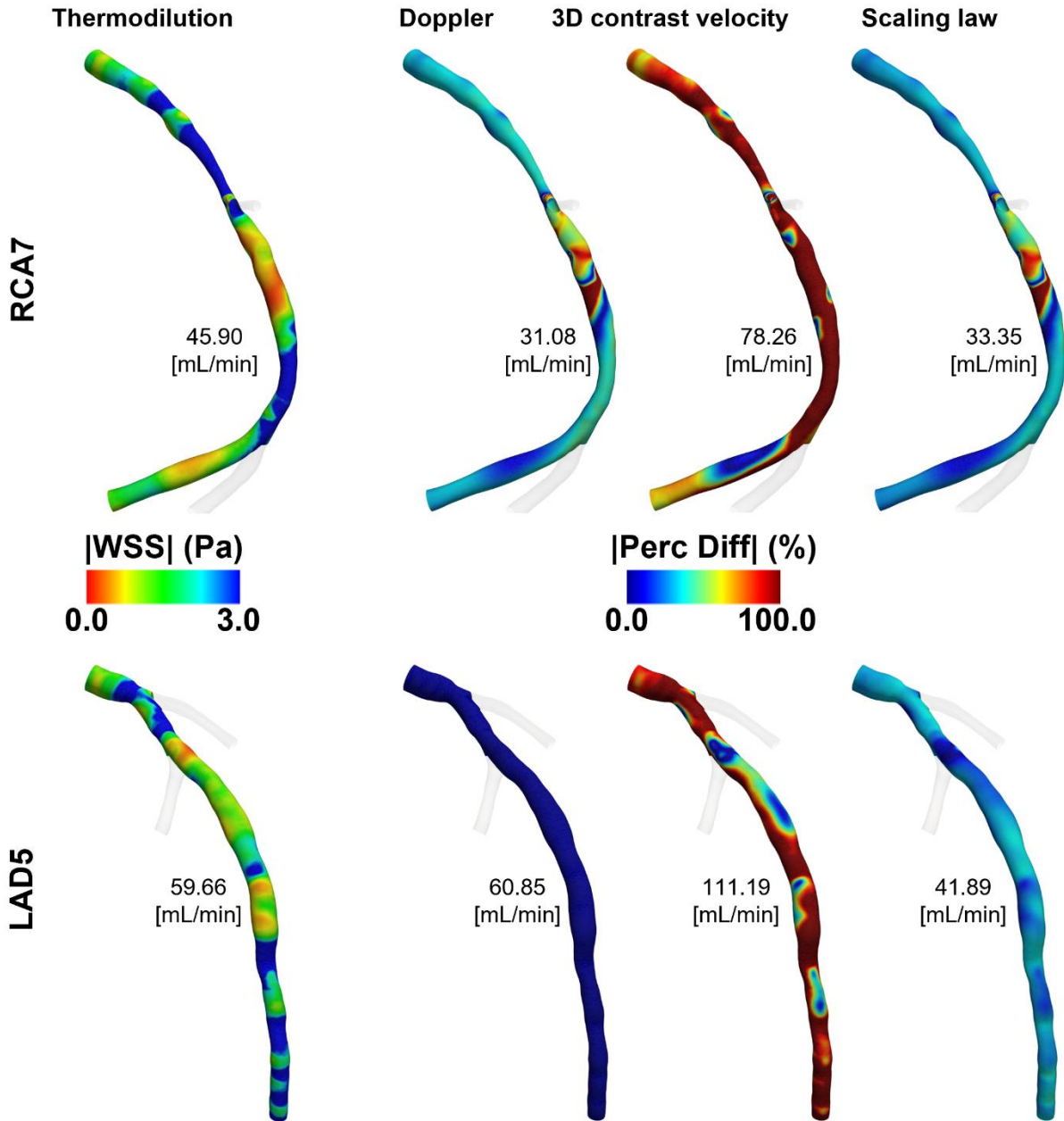
Figure 3. WSS magnitude distribution at the luminal surface for the reference inflow boundary condition thermodilution (left panel). Distribution of absolute values of WSS magnitude percentage differences of Doppler-based, 3D contrast velocity-based and scaling law-based vs. thermodilution-based flow rate values (right panel). Two explanatory cases, one LAD and one RCA, are reported.
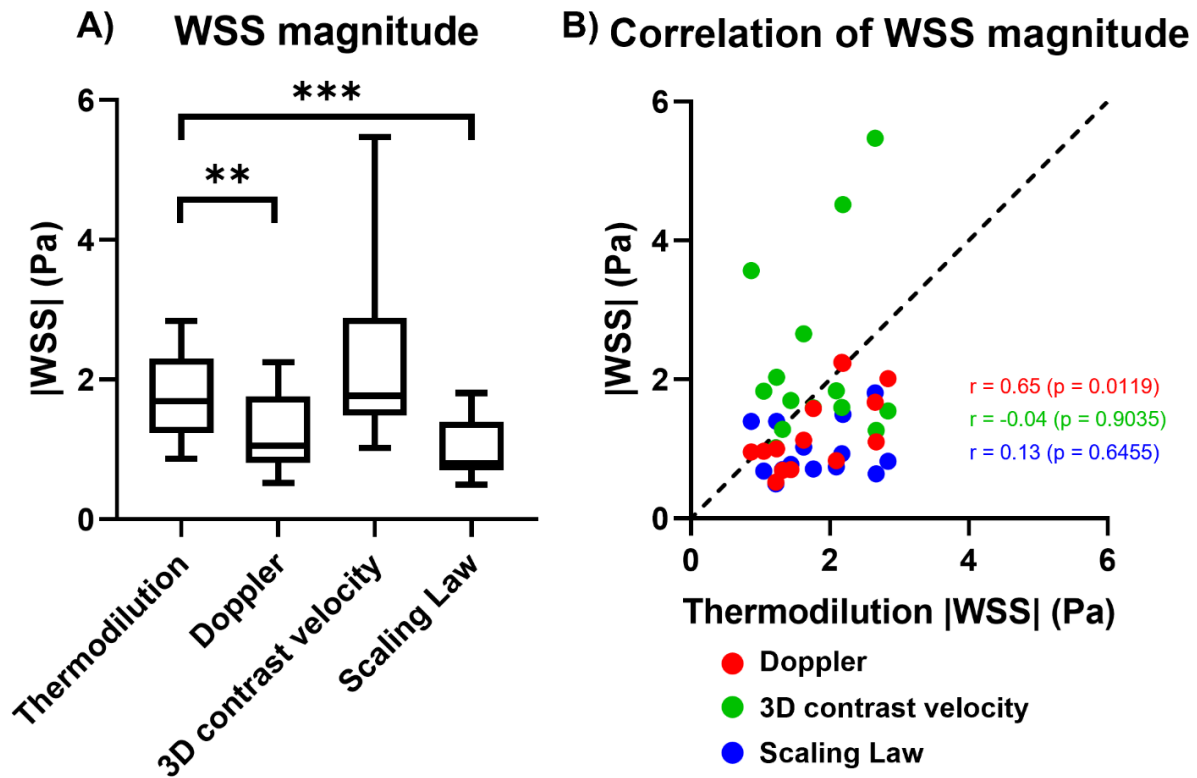
Figure 4. (A) boxplot representation of luminal surface-averaged WSS magnitude values per adopted technique. Statistically significant differences between obtained from thermodilution-based flow rate assessment and the three other techniques are indicated with ** (p<0.01) and *** (p<0.001); (B) scatter plots of thermodilution-based luminal surface-averaged WSS magnitude values vs. Doppler-based, 3D contrast velocity-based and scaling law-based ones. The black dotted line represents the identity line.

As for the luminal surface areas exposed to low WSS magnitude, no significant differences emerged applying the different flow rate values as inflow BC (**Figure 5A**). Additionally, the analysis of WSS10 surface areas highlighted a satisfactory co-localization (**Figure 5B**) of the results from Q_{thermo}-based simulations with $Q_{Doppler}$-based (SI = 0.67 [0.49-0.83]), Q_{CV}-based (SI = 0.64 [0.51-0.84]) and Q_{SL}-based (SI = 0.69 [0.39-0.79]) simulations. Explanatory WSS10 co-localization maps are presented in **Figure 5C**, where the two cases with the lowest and highest SI value are displayed.
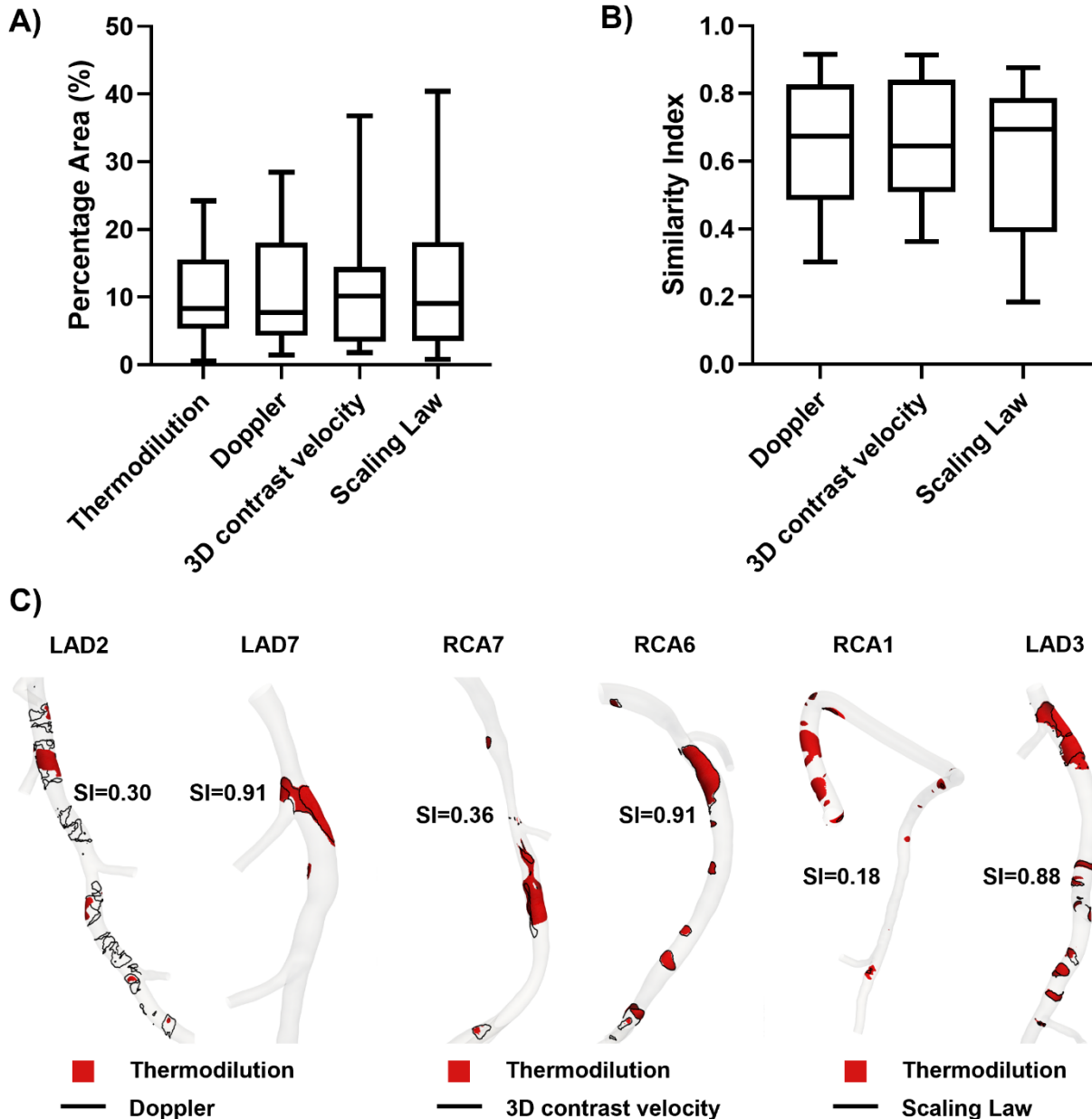
Figure 5. (A) boxplot representation of luminal surface percentage area exposed to low WSS per adopted technique; B) boxplot representation of the luminal surface area exposed to low WSS magnitude of Doppler-based, 3D contrast velocity-based, and scaling law-based simulations co-localizing with low WSS magnitude surface area of thermodilution-based simulations, expressed in terms of similarity index (SI); (C) visual representation of the co-localization of the luminal surface areas exposed to low WSS magnitude in Doppler-based, 3D contrast velocity-based, and scaling law-based simulations with respect to thermodilution-based simulations. For each flow rate assessment technique, the two cases with highest and lowest SI, are presented.

When considering surface-averaged values of normalized WSS, significant albeit moderate differences emerged between simulations based on Q_{thermo} and $Q_{Doppler}$ as inflow BC (1.18 [0.99 -1.81] and 1.07 [0.92-1.81], respectively; p=0.0101) and simulations based on Q_{thermo}

18

and Q_{SL} (1.04 [0.89-1.93]; p=0.0203) as inflow BC (**Figure 6A**). Very strong linear

correlations emerged between surface-averaged normalized WSS magnitude median

values derived from $Q_{Doppler}$-based, Q_{CV}-based and Q_{SL}-based simulations and Q_{thermo}-based

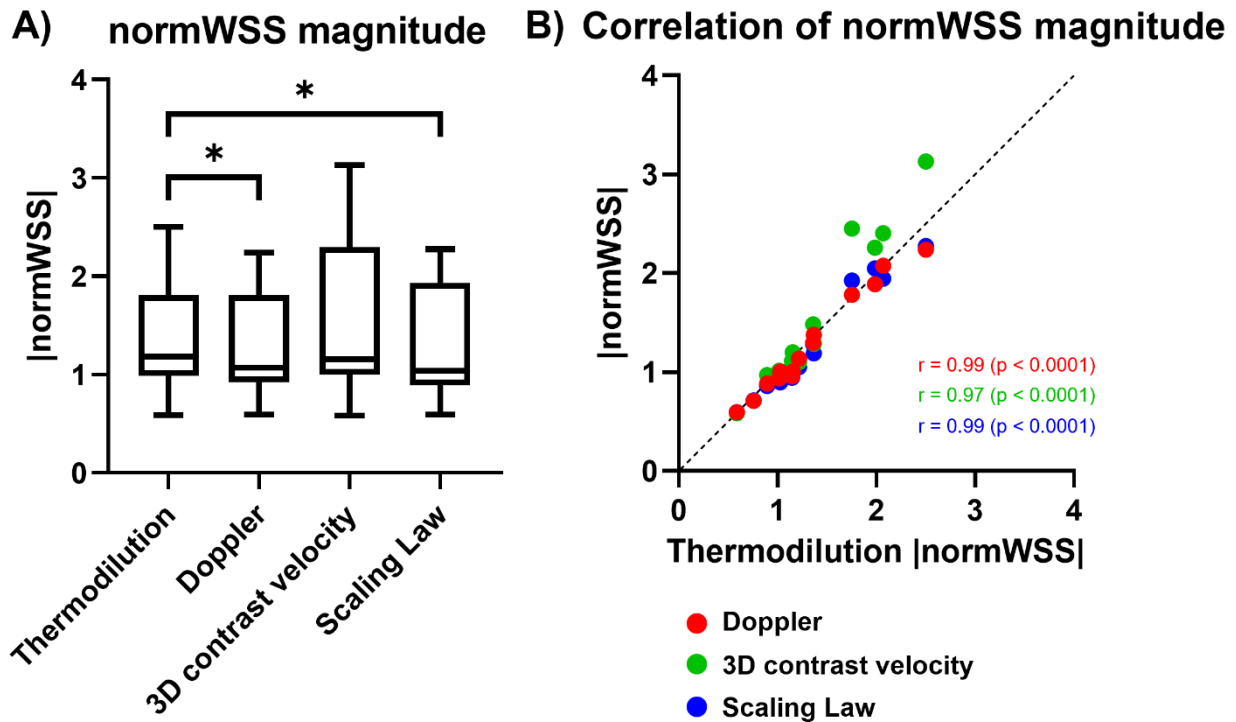simulations (r>0.97 and p<0.0001 in all cases, **Figure 6B**).

Figure 6. (A) boxplot representation of luminal surface-averaged normalized WSS (normWSS) magnitude values per adopted technique. Statistically significant differences between obtained from thermodilution-based flow rate assessment and the three other techniques are indicated with * (p<0.05); (B) scatter plots of thermodilution-based luminal surface-averaged normalized WSS magnitude values vs. Doppler-based, 3D contrast velocity-based and scaling law-based ones. The black dotted line represents the identity line.

The impact of the different flow rates adopted as inflow BCs on WSS directionality was

overall low: the 90th percentile values of the AEWSSD values probability density function

were equal to 0.0095, 0.0105, and 0.0194, for $Q_{Doppler}$-based, Q_{CV}-based, and Q_{SL}-based

simulations, corresponding to local misalignments of WSS vectors from the reference (from

Q_{thermo}-based simulations) equal to 0.5443°, 0.6016°, and 1.1116°, respectively (**Figure 7A**).

By visual inspection of the AEWSSD luminal surface distributions of two representative

cases characterized by the absence/presence of regions of markedly different WSS

19

misalignment, it was possible to observe that WSS misalignment was located close to the side branches, i.e., where the WSS deviation from the axial direction is more pronounced (model LAD6 in **Figure 7B**).

The correlation between steady-state WSS-magnitude profiles and TAWSS profiles from unsteady state simulations (**Supplementary Figure 3**) was very strong ($r \geq 0.998$; $p < 0.0001$), proving that here analysed steady-state WSS magnitude values are representative of the cycle-average WSS magnitude.
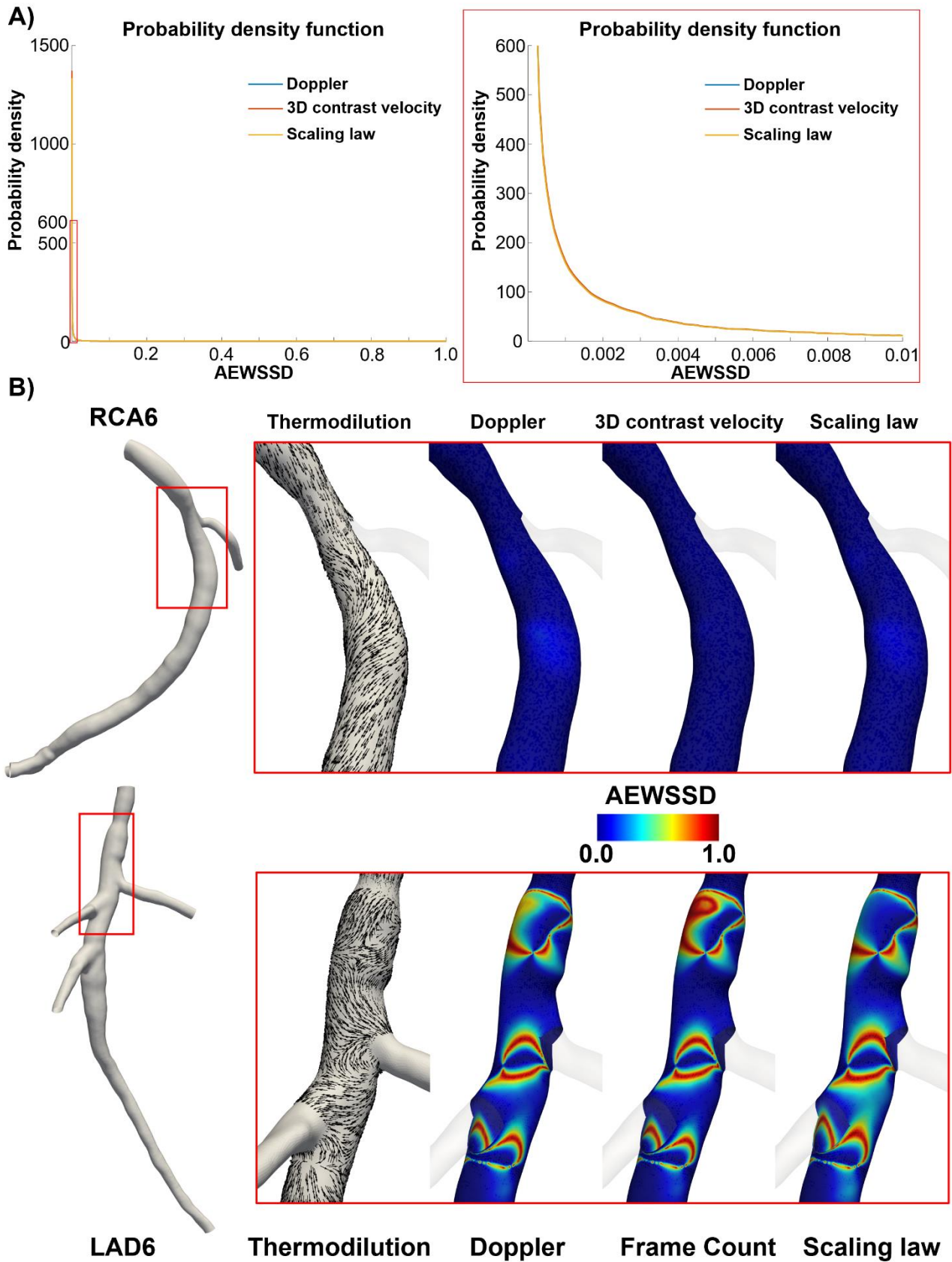
Figure 7. (A) probability density function of the absolute error in WSS direction (AEWSSD) with an inset zooming in AEWSSD values < 90th percentile; (B) zoomed visualizations (red box) of the WSS normalized vector field obtained from Doppler-based, 3D contrast velocity-based, and scaling law-based simulations with respect to the thermodilution-based one. Two explanatory cases, one with low and one with high AEWSSD values, are presented.

Impact of flow rate estimation on coronary helical flow

Intravascular flow visualization using LNH isosurfaces highlighted the establishment of distinguishable counter-rotating helical blood flow patterns in the coronary models (**Supplementary Figure 4** and **Figure 8**). In all cases, helical flow is topologically similar, independent of the flow rate estimate applied as inflow BC.

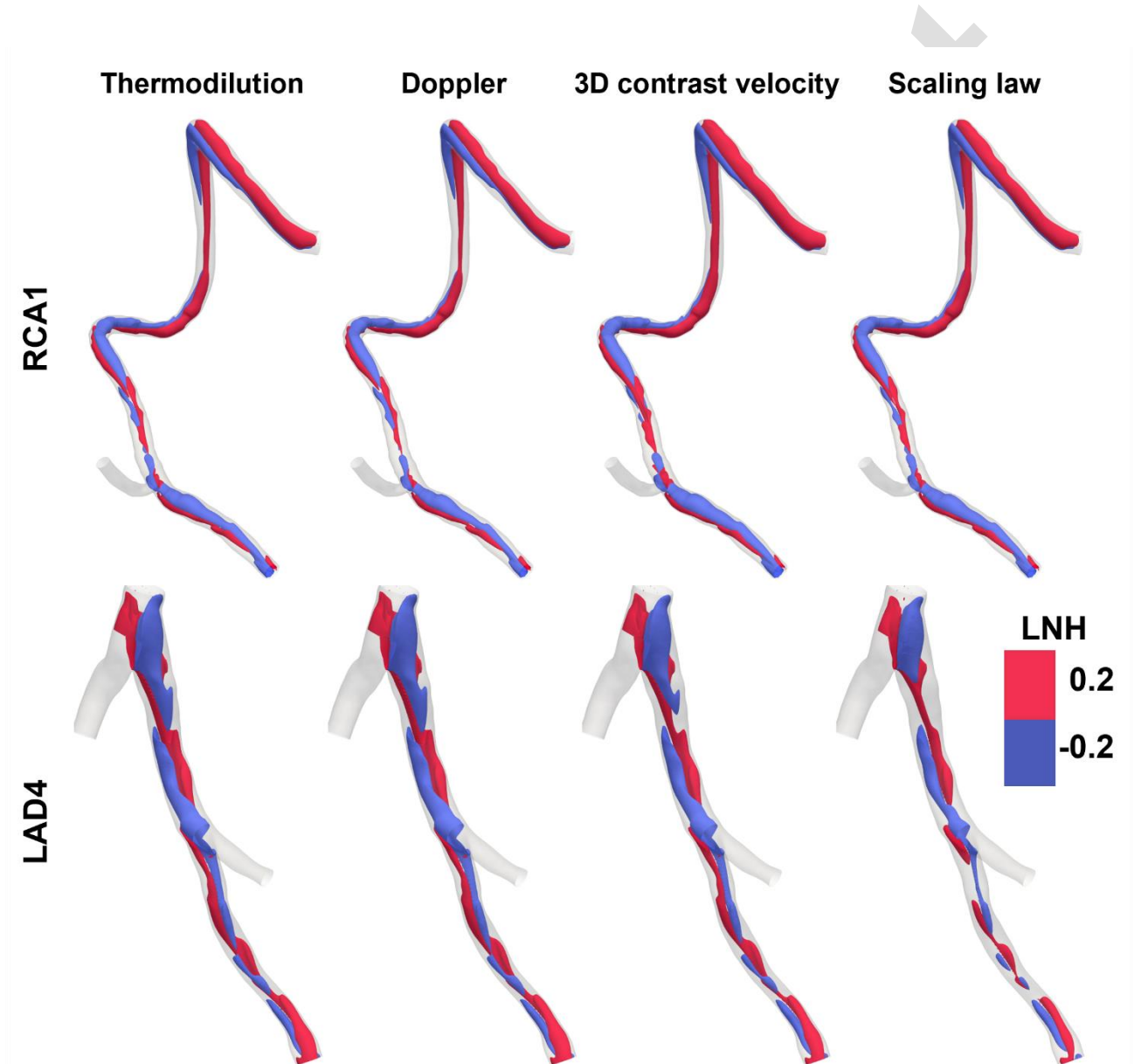**Figure 8.** Visualization of intravascular local normalized helicity (LNH) isosurfaces for two explanatory cases (one RCA and one LAD). Right-handed helical structures are associated with positive LNH values (red colour), and left-handed helical structures are associated with negative LNH values (blue colour). In general, the helical flow topology is independent of the flow rate inflow BC-based strategy.

The impact of the different flow rate estimates prescribed as inflow BC on coronary helical flow features is quantified in **Figure 9A**. Helicity production intensity was sensitive to the inlet flow rate. Overall, Q_{CV}-based simulations presented the highest h_2 values as well as the largest range of variation (h_2 = 7.48 [3.56-15.89] m/s^2), although the differences with respect to the Q_{thermo}-based simulations were not significant (h_2 = 5.87 [3.23-8.66] m/s^2). Conversely, significant differences with respect to the Q_{thermo}-based simulations emerged for the $Q_{Doppler}$-based (h_2 = 1.71 [0.88-5.72] m/s^2, p=0.0023) and Q_{SL}-based simulations (h_2 = 1.09 [0.62-3.00] m/s^2, p=0.0012). Differences from Q_{thermo}-based simulations emerged also in terms bi-helical flow patterns balance, expressed in terms of h_3 and h_4. In particular, a significant but weak difference was found between the simulations based on $Q_{doppler}$ and Q_{thermo} in terms of h_3 (0.03 [-0.06-0.13] and 0.02 [-0.05-0.07], respectively; p<0.0350). A more significant difference emerged between the simulations based on Q_{SL} and Q_{thermo} in terms of h_4 (0.06 [0.04-0.09] and 0.09 [0.06-0.14], respectively; p=0.0183). However, such differences in helical flow topological organization can be considered negligible, with h_3 and h_4 tending to be a simple affair round the zero value, the latter indicating perfect balance of counter-rotating helical flow patterns. As far as the whole helicity production (h_1), no significant differences from Q_{thermo}-based simulations emerged (**Figure 9A**). Results of the linear correlation analysis for the helicity-based descriptors are presented in **Figure 9B**. Descriptor h_1 from Q_{CV}-based and Q_{SL}-based simulations was correlated (even if not very strongly) with the same descriptor obtained from Q_{thermo}-based simulations (r=0.60, 95% CI 0.10 to 0.86; p=0.0235 and r=0.55, 95% CI 0.01 to 0.84; p=0.0438, respectively). Regarding h_2, a significant linear correlation between Q_{thermo}-based and $Q_{Doppler}$-based simulations (r=0.53, 95% CI 0.00 to 0.83; p=0.0496) emerged. Descriptor h_3 from $Q_{Doppler}$-based, Q_{CV}-based and Q_{SL}-based simulations were strongly correlated with the same descriptors obtained from Q_{thermo}-based simulations (r>0.92 and p<0.0001 in all cases) (**Figure 9B**),

23

confirming that different flow rate estimates applied as inflow BCs have a more marked impact on helicity intensity rather than on helical flow topological features.
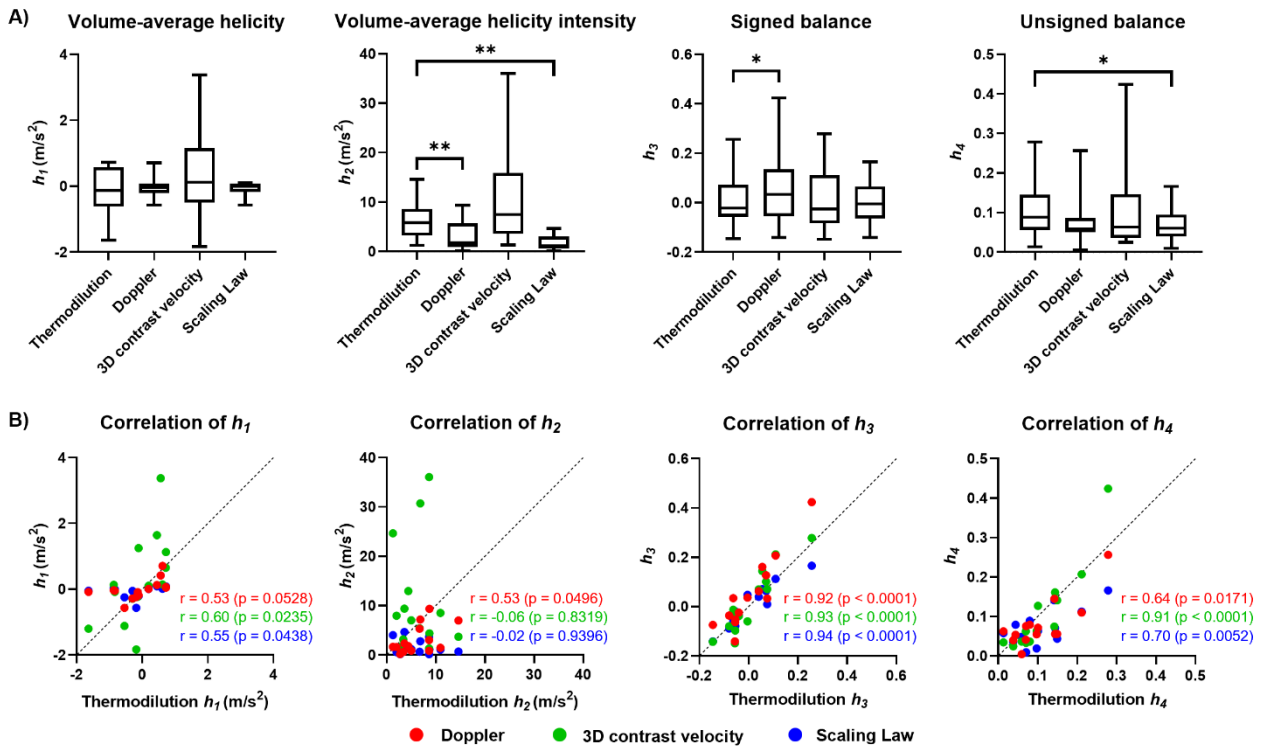

Figure 9. (A) boxplot representation of helicity-based descriptors distributions per adopted technique. Statistically significant differences, evaluated between thermodilution and the other flow rate assessment techniques, are indicated with * (p<0.05) and ** (p<0.01); (B) scatter plots of helicity-based descriptors from thermodilution-based vs. Doppler-based, 3D contrast velocity-based and scaling law-based flow rate assessment. r and p are the correlation coefficient and the p-value of the linear regression, and the black dotted line represents the identity line.

The correlation between steady- and unsteady-state helicity-based descriptors (**Supplementary Figure 5**) was very strong (r≥0.928; p<0.0001), proving that steady-state helicity-based descriptors capture the main features of cycle-averaged helical flow patterns.

24

Discussion

The present study performed a comparative analysis among four different techniques for the *in vivo* assessment of coronary blood flow rate, namely continuous thermodilution, intravascular Doppler flow, 3D contrast velocity and anatomy-based scaling law. The analysis was carried out in terms of assessed blood flow rate values, and angiography-based CFD simulations of the coronary hemodynamics with inflow BCs derived from the four different techniques.

The main findings of the present study can be summarised as follows: (1) coronary flow rate value may vary across *in vivo* measurement techniques, given that the clinically available techniques are based on different theories as well as practical approaches; (2) differences in measured blood flow rates reflect into uncertainty on the prescribed inflow BCs for angiography-based CFD simulations, which in turn can impact both local WSS distribution and intravascular flow patterns, such as intracoronary helical flow.

The rationale of this work lies in the evaluation of the endothelial shear stress based on the integration of patient data and CFD simulations. In the context of coronary atherosclerosis, endothelial shear stress promises to have a remarkable translational clinical impact, by virtue of its ability to identify e.g. coronary segments with endothelial dysfunction [47], intermediate coronary lesion prone to rupture [11,48], and site of subsequent myocardial infarction [10]. To pursue the goal of using CFD models of coronary arteries to inform (and possibly enable) prognosis and preemptive treatment strategies, the available clinical information should be leveraged to determine the conditions to be prescribed at the inflow boundaries, which represent a major source of uncertainty.

The here investigated clinically implementable approaches for flow rate assessment in coronary arteries are characterized by different levels of invasiveness, uncertainty, and

costs. Among them, only continuous thermodilution provides a direct measurement of blood flow rate, independent of the 3D reconstruction of the vessel. Moreover, previous studies reported continuous thermodilution being less sensitive to loading conditions, wire position, and accounting for a lower interoperator variability with respect to e.g. Doppler flow measurements, which remain difficult to perform [28,49,50]. These considerations motivated the adoption of continuous thermodilution as reference technique in the present analysis. Differently from the latter, the estimation of the blood flow rate values by the other three techniques might be affected also by the uncertainties related to the geometric reconstruction. As evident from equations 2, 3 and 4, all analysed techniques with the exception of continuous thermodilution require the estimation of the cross-sectional lumen area or the hydraulic diameter to obtain the blood flow rate value, with an associated budget of uncertainty ascribable to (i) the quality of images recorded within the routine clinical framework, (ii) the reconstruction methods (e.g. using two angiographic views) [51] and (iii) the location where the cross section is considered, as local variations may be present due to tapering and geometric complexity. Moreover, the conversion of the Doppler velocity measurement to flow rate values necessarily requires an assumption on the velocity profile (e.g., parabolic) that may affect the reliability of the estimated flow rate value [23,52]. The 3D contrast velocity method and the anatomy-based scaling law represent the two most clinically convenient techniques since they make use of angiography alone. However, for the former the sensitivity of the estimated flow rate value to the angiographic images acquisition frame rate (i.e., parameter f in equation 3) might be remarkable. For the latter, the flow rate estimation depends on the local hydraulic diameter solely. Moreover, a previous comparison with intravascular Doppler ultrasound measurements [53] underlined how the application of the scaling law, represented by eq. (4), leads to a general underestimation of both flow rate and WSS values, as also observed in the present study (**Figures 2** and **4**). Since eq. (4) was derived from Doppler velocity measurements in angiographically normal

bifurcations of patients presenting with coronary artery disease, it may not properly account for the influence of the resistance of the distal vascular bed, with a possible impact on the observed relationship between geometry and flow rate [27].

The here observed significant correlation between Q_{thermo} and $Q_{Doppler}$ (**Figure 2C**) is consistent with recent studies on animals and humans reporting a satisfactory agreement between Doppler flow-based and thermodilution-based measurements of blood flow [28] or coronary flow reserve (CFR) [54,55], defined as the ratio of coronary flow in hyperemic conditions to resting coronary flow. Conversely, contradictory findings have been reported when comparing TIMI frame count-based and Doppler flow-based CFR [56,57].

Not unexpectedly, on one hand the differences here observed in the flow rate assessment are reflected on the WSS magnitude profile (**Figures 2** and **4**), in agreement with previous studies [53,58]. The significance of these differences decreased when considering normalized WSS values, while a very strong linear correlation with respect to the Q_{thermo}-based simulation emerged for all cases (**Figure 6**). This expands the previously reported lower sensitivity of normalized WSS with respect to absolute WSS values when comparing inflow BCs based on intravascular Doppler measurements *vs.* the anatomy-based scaling law adopted here [22]. This would seem to suggest that the use of normalized WSS would help increase standardization, although the biological and clinical implications of absolute *vs.* normalized WSS need to be elucidated. On the other hand, the surface area exposed to low WSS magnitude values is less sensitive to the flow rate prescribed at the inlet section, as no significant differences in WSS10 emerged among simulation with different inflow BCs (**Figure 5**). Recent evidence demonstrated that the adoption of a study-specific threshold to define low WSS, as done here, may not compromise the predictive power of WSS for coronary plaque progression [59]. In this sense, the robustness of the surface area exposed to low WSS could allow to reliably stratify subjects at risk of developing coronary

27

atherosclerosis even when intravascular flow measurements are not available, such as in retrospective studies.

Regarding the impact of blood flow rate on coronary helical flow features with a recognized atheroprotective role [12,13], the impact of the prescribed inflow BC is more relevant for the helicity intensity, quantified by h_2. In detail, the results obtained from the statistical analysis of h_2 for the four analysed inflow BCs match what observed for the absolute flow rate and WSS magnitude. This can be explained by the established correlation between helicity intensity and WSS magnitude in coronary arteries [12], and the dependence by construction of h_2 on the velocity magnitude (Eq. 9). Conversely, helical flow topology (**Figure 8**) appeared to be limitedly affected by the prescribed flow rate value applied as inflow BC, suggesting that coronary geometry is a more important determinant of helical flow topology than the inflow BC.

Finally, the strong correlation between steady-state WSS-magnitude profiles and TAWSS or helicity-based descriptors from unsteady state simulations proves that the findings on steady-state WSS magnitude are representative of the cycle-average quantities characterizing unsteady-state simulations.

Limitations

Several limitations could weaken the findings of this study. The volume of saline infused for the continuous thermodilution measurements might influence the flow rate values. However, a previous study indicated that the infusion rate adopted here did not affect flow velocity [29]. In this study, steady-state simulations were carried out, neglecting the pulsatile nature of coronary flow. However, the strong significant correlation between TAWSS vs. steady-state WSS magnitude (**Supplementary Figure 3**), and unsteady- *vs.* steady-state helicity-based descriptors (**Supplementary Figure 5**) support our choice, corroborating results from previous studies [11,60]. Moreover, the flow rate values at the inflow section were imposed

28

as a Dirichlet boundary condition in terms of a parabolic velocity profile. We reasonably expect a limited effect of the inflow velocity profile on the simulated hemodynamics based on our previous findings demonstrating that the influence of the inlet velocity profile shape in LADs vanishes after a length equal to few inlet cross-section diameters [33]. The adopted outflow boundary conditions based on a prescribed flow split at each coronary bifurcation according to a diameter-based scaling law might influence the simulated hemodynamics. However, at this stage of the investigation, the lack of measured patient-specific flow split does not entail the generality of the results.

Conclusions

In this study, different clinically applicable techniques for flow rate measurements in coronary arteries were compared and their impact on the results obtained when blood flow rate measurements are used to derive personalized inflow BCs in computational hemodynamics models was evaluated. Our findings indicate that the flow rate values provided by the different measurement techniques may reflect into different WSS profiles as well as helical blood flow intensity. However, such differences are not significant in terms of luminal surface area exposed to low WSS magnitude as well as in terms of helical flow topological features. Given the obtained results and the fact that it is uncommon to have patient-specific measured flow rates in the clinical practice, we refrain from a general recommendation for one coronary flow measurement technique, highlighting the uncertainty associated with assumptions related to inflow BCs. This suggests that particular attention should be given in analysing results obtained from patient-specific CFD simulations in coronary arteries and that a standardization would be desirable to provide comparable results among different studies, while waiting for the improvement and wider dissemination of non-invasive and precise flow rate measurement [61].

Declarations

Conflicts of interest

The authors declare that they have no conflict of interest.

Authors' contribution

Conceptualization: MLR, DG, UM; Data Acquisition and Organization: AC, EG, BDB, TM, CCo; 3D reconstructions: MLR; CFD simulations: MLR, KC; Statistical Analyses: MLR; Supervision: DG, UM; Writing - Original Draft Preparation: MLR, AC, CCh, DG, UM; Writing - Review & Editing: MLR, AC, CCh, EG, KC, FDA, BDB, CC, DG, UM. All authors discussed the results and reviewed the manuscript.

Bibliography

[1]   U. Morbiducci, A.M. Kok, B.R. Kwak, P.H. Stone, D.A. Steinman, J.J. Wentzel, Atherosclerosis at arterial bifurcations: Evidence for the role of haemodynamics and geometry, Thromb. Haemost. 115 (2016) 484–492. https://doi.org/10.1160/TH15-07-0597.

[2]   C. Souilhol, J. Serbanovic-Canic, M. Fragiadaki, T.J. Chico, V. Ridger, H. Roddie, P.C. Evans, Endothelial responses to shear stress in atherosclerosis: a novel role for developmental genes, Nat. Rev. Cardiol. 17 (2020) 52–63. https://doi.org/10.1038/s41569-019-0239-5.

[3]   Y. Alexander, E. Osto, A. Schmidt-Trucksäss, M. Shechter, D. Trifunovic, D.J. Duncker, V. Aboyans, M. Bäck, L. Badimon, F. Cosentino, M. De Carlo, M. Dorobantu, D.G. Harrison, T.J. Guzik, I. Hoefer, P.D. Morris, G.D. Norata, R. Suades, S. Taddei, G. Vilahur, J. Waltenberger, C. Weber, F. Wilkinson, M.L. Bochaton-Piallat, P.C. Evans, Endothelial function in cardiovascular medicine: A consensus paper of the European Society of Cardiology Working Groups on Atherosclerosis and Vascular Biology, Aorta and Peripheral Vascular Diseases, Coronary Pathophysiology and Microcirculation, and Thr, Cardiovasc. Res. 117 (2021) 29–42. https://doi.org/10.1093/cvr/cvaa085.

[4]   C. V Bourantas, T. Zanchin, R. Torii, P.W. Serruys, A. Karagiannis, A. Ramasamy, H. Safi, A.U. Coskun, G. Koning, Y. Onuma, C. Zanchin, R. Krams, A. Mathur, A. Baumbach, G. Mintz, S. Windecker, A. Lansky, A. Maehara, P.H. Stone, L. Raber, G.W. Stone, Shear Stress Estimated by Quantitative Coronary Angiography Predicts Plaques Prone to Progress and Cause Events., JACC. Cardiovasc. Imaging. 13 (2020) 2206–2219. https://doi.org/10.1016/j.jcmg.2020.02.028.

[5] V. Mazzi, G. De Nisco, A. Hoogendoorn, K. Calò, C. Chiastra, D. Gallo, D.A. Steinman, J.J. Wentzel, U. Morbiducci, Early Atherosclerotic Changes in Coronary Arteries are Associated with Endothelium Shear Stress Contraction/Expansion Variability., Ann. Biomed. Eng. 49 (2021) 2606–2621. https://doi.org/10.1007/s10439-021-02829-5.

[6] A. Hoogendoorn, A.M. Kok, E.M.J. Hartman, G. De Nisco, L. Casadonte, C. Chiastra, A. Coenen, S.A. Korteland, K. Van der Heiden, F.J.H. Gijsen, D.J. Duncker, A.F.W. Van der Steen, J.J. Wentzel, Multidirectional wall shear stress promotes advanced coronary plaque development: Comparing five shear stressmetrics, Cardiovasc. Res. 116 (2021) 1136–1146. https://doi.org/10.1093/CVR/CVZ212.

[7] Y.S. Chatzizisis, A.U. Coskun, M. Jonas, E.R. Edelman, C.L. Feldman, P.H. Stone, Role of Endothelial Shear Stress in the Natural History of Coronary Atherosclerosis and Vascular Remodeling. Molecular, Cellular, and Vascular Behavior, J. Am. Coll. Cardiol. 49 (2007) 2379–2393. https://doi.org/10.1016/j.jacc.2007.02.059.

[8] P.H. Stone, S. Saito, S. Takahashi, Y. Makita, S. Nakamura, T. Kawasaki, A. Takahashi, T. Katsuki, S. Nakamura, A. Namiki, A. Hirohata, T. Matsumura, S. Yamazaki, H. Yokoi, S. Tanaka, S. Otsuji, F. Yoshimachi, J. Honye, D. Harwood, M. Reitman, A.U. Coskun, M.I. Papafaklis, C.L. Feldman, Prediction of progression of coronary artery disease and clinical outcomes using vascular profiling of endothelial shear stress and arterial plaque characteristics: The PREDICTION study, Circulation. 126 (2012) 172–181. https://doi.org/10.1161/CIRCULATIONAHA.112.096438.

[9] H. Samady, P. Eshtehardi, M.C. McDaniel, J. Suo, S.S. Dhawan, C. Maynard, L.H.

Timmins, A.A. Quyyumi, D.P. Giddens, Coronary artery wall shear stress is associated with progression and transformation of atherosclerotic plaque and arterial remodeling in patients with coronary artery disease, Circulation. 124 (2011) 779–788. https://doi.org/10.1161/CIRCULATIONAHA.111.021824.

[10] A. Candreva, M. Pagnoni, M.L. Rizzini, T. Mizukami, E. Gallinoro, V. Mazzi, D. Gallo, D. Meier, T. Shinke, J.P. Aben, S. Nagumo, J. Sonck, D. Munhoz, S. Fournier, E. Barbato, W. Heggermont, S. Cook, C. Chiastra, U. Morbiducci, B. De Bruyne, O. Muller, C. Collet, Risk of myocardial infarction based on endothelial shear stress analysis using coronary angiography, Atherosclerosis. (2021). https://doi.org/10.1016/j.atherosclerosis.2021.11.010.

[11] A. Kumar, E.W. Thompson, A. Lefieux, D.S. Molony, E.L. Davis, N. Chand, S. Fournier, H.S. Lee, J. Suh, K. Sato, Y.A. Ko, D. Molloy, K. Chandran, H. Hosseini, S. Gupta, A. Milkas, B. Gogas, H.J. Chang, J.K. Min, W.F. Fearon, A. Veneziani, D.P. Giddens, S.B. King, B. De Bruyne, H. Samady, High Coronary Shear Stress in Patients With Coronary Artery Disease Predicts Myocardial Infarction, J. Am. Coll. Cardiol. 72 (2018) 1926–1935. https://doi.org/10.1016/j.jacc.2018.07.075.

[12] G. De Nisco, A.M. Kok, C. Chiastra, D. Gallo, A. Hoogendoorn, F. Migliavacca, J.J. Wentzel, U. Morbiducci, The Atheroprotective Nature of Helical Flow in Coronary Arteries, Ann. Biomed. Eng. 47 (2019) 425–438. https://doi.org/10.1007/s10439-018-02169-x.

[13] G. De Nisco, A. Hoogendoorn, C. Chiastra, D. Gallo, A.M. Kok, U. Morbiducci, J.J. Wentzel, The impact of helical flow on coronary atherosclerotic plaque development, Atherosclerosis. 300 (2020) 39–46. https://doi.org/10.1016/j.atherosclerosis.2020.01.027.

[14] R. Pandey, M. Kumar, J. Majdoubi, M. Rahimi-Gorji, V.K. Srivastav, A review study on blood in human coronary artery: Numerical approach, Comput. Methods Programs Biomed. 187 (2020) 1–12. https://doi.org/10.1016/j.cmpb.2019.105243.

[15] V. Carvalho, D. Pinho, R.A. Lima, J.C. Teixeira, S. Teixeira, Blood flow modeling in coronary arteries: A review, Fluids. 6 (2021). https://doi.org/10.3390/fluids6020053.

[16] S. Sankaran, H.J. Kim, G. Choi, C.A. Taylor, Uncertainty quantification in coronary blood flow simulations: Impact of geometry, boundary conditions and blood viscosity, J. Biomech. 49 (2016) 2540–2547. https://doi.org/10.1016/j.jbiomech.2016.01.002.

[17] S. Bozzi, U. Morbiducci, D. Gallo, R. Ponzini, G. Rizzo, C. Bignardi, G. Passoni, Uncertainty propagation of phase contrast-MRI derived inlet boundary conditions in computational hemodynamics models of thoracic aorta, Comput. Methods Biomech. Biomed. Engin. 20 (2017) 1104–1112. https://doi.org/10.1080/10255842.2017.1334770.

[18] D.A. Steinman, F. Migliavacca, Editorial: Special Issue on Verification, Validation, and Uncertainty Quantification of Cardiovascular Models: Towards Effective VVUQ for Translating Cardiovascular Modelling to Clinical Utility, Cardiovasc. Eng. Technol. 9 (2018) 539–543. https://doi.org/10.1007/s13239-018-00393-z.

[19] C.M. Fleeter, G. Geraci, D.E. Schiavazzi, A.M. Kahn, A.L. Marsden, Multilevel and multifidelity uncertainty quantification for cardiovascular hemodynamics., Comput. Methods Appl. Mech. Eng. 365 (2020). https://doi.org/10.1016/j.cma.2020.113030.

[20] G. Ninos, V. Bartzis, N. Merlemis, I.E. Sarris, Uncertainty quantification implementations in human hemodynamic flows, Comput. Methods Programs Biomed. 203 (2021) 106021. https://doi.org/10.1016/j.cmpb.2021.106021.

[21] M. Lodi Rizzini, D. Gallo, G. De Nisco, F. D'Ascenzo, C. Chiastra, P.P. Bocchino, F.

Piroli, G.M. De Ferrari, U. Morbiducci, Does the inflow velocity profile influence physiologically relevant flow patterns in computational hemodynamic models of left anterior descending coronary artery?, Med. Eng. Phys. 82 (2020) 58–69. https://doi.org/10.1016/j.medengphy.2020.07.001.

[22] J.T.C. Schrauwen, J.C.V. Schwarz, J.J. Wentzel, A.F.W. Van Der Steen, M. Siebes, F.J.H. Gijsen, The impact of scaled boundary conditions on wall shear stress computations in atherosclerotic human coronary bifurcations, Am. J. Physiol. - Hear. Circ. Physiol. 310 (2016) H1304–H1312. https://doi.org/10.1152/ajpheart.00896.2015.

[23] J.W. Doucette, P.D. Corl, H.M. Payne, A.E. Flynn, M. Goto, M. Nassi, J. Segal, Validation of a Doppler guide wire for intravascular measurement of coronary artery flow velocity, Circulation. 85 (1992) 1899–1911. https://doi.org/10.1161/01.CIR.85.5.1899.

[24] C.M. Gibson, C.P. Cannon, W.L. Daley, J.T. Dodge, B. Alexander, S.J. Marble, C.H. McCabe, L. Raymond, T. Fortin, W.K. Poole, E. Braunwald, TIMI Frame Count , Circulation. 93 (1996) 879–888. https://doi.org/10.1161/01.CIR.93.5.879.

[25] S. Tu, E. Barbato, Z. Köszegi, J. Yang, Z. Sun, N.R. Holm, B. Tar, Y. Li, D. Rusinaru, W. Wijns, J.H.C. Reiber, Fractional flow reserve calculation from 3-dimensional quantitative coronary angiography and TIMI frame count: A fast computer model to quantify the functional significance of moderately obstructed coronary arteries, JACC Cardiovasc. Interv. 7 (2014) 768–777. https://doi.org/10.1016/j.jcin.2014.03.004.

[26] C.D. Murray, The Physiological Principle of Minimum Work: I. The Vascular System and the Cost of Blood Volume., Proc. Natl. Acad. Sci. U. S. A. 12 (1926) 207–214.

https://doi.org/10.1073/pnas.12.3.207.

[27] A.G. van der Giessen, H.C. Groen, P.A. Doriot, P.J. de Feyter, A.F.W. van der Steen, F.N. van de Vosse, J.J. Wentzel, F.J.H. Gijsen, The influence of boundary conditions on wall shear stress distribution in patients specific coronary trees, J. Biomech. 44 (2011) 1089–1095. https://doi.org/10.1016/j.jbiomech.2011.01.036.

[28] W. Aarnoudse, M. van't Veer, N.H.J. Pijls, J. ter Woorst, S. Vercauteren, P. Tonino, M. Geven, M. Rutten, E. van Hagen, B. de Bruyne, F. van de Vosse, Direct Volumetric Blood Flow Measurement in Coronary Arteries by Thermodilution, J. Am. Coll. Cardiol. 50 (2007) 2294–2304. https://doi.org/10.1016/j.jacc.2007.08.047.

[29] E. Gallinoro, A. Candreva, I. Colaiori, M. Kodeboina, S. Fournier, O. Nelis, G. Di Gioia, J. Sonck, M. van 't Veer, N.H.J. Pijls, C. Collet, B. De Bruyne, Thermodilution-derived volumetric resting coronary blood flow measurement in humans, EuroIntervention. 17 (2021) e672–e679. https://doi.org/10.4244/EIJ-D-20-01092.

[30] A. Candreva, E. Gallinoro, M. van 't Veer, J. Sonck, C. Collet, G. Di Gioia, M. Kodeboina, T. Mizukami, S. Nagumo, D. Keulards, S. Fournier, N.H.J. Pijls, B. De Bruyne, Basics of Coronary Thermodilution, JACC Cardiovasc. Interv. 14 (2021) 595–605. https://doi.org/10.1016/j.jcin.2020.12.037.

[31] M.A. Kelshiker, H. Seligman, J.P. Howard, H. Rahman, M. Foley, A.N. Nowbar, C.A. Rajkumar, M.J. Shun-Shin, Y. Ahmad, S. Sen, R. Al-Lamee, R. Petraco, G. Cole, S.P. Hoole, P.D. Morris, F. Rigo, D.P. Francis, J. Mayet, Coronary flow reserve and cardiovascular outcomes: a systematic review and meta-analysis, Eur. Heart J. (2021) 1–15. https://doi.org/10.1093/eurheartj/ehab775.

[32] R.E. Konst, S.E. Elias-Smale, D. Pellegrini, M. Hartzema-Meijer, B.J.C. van Uden, T.P.J. Jansen, P. Vart, H. Gehlmann, A.H.E.M. Maas, N. van Royen, P. Damman,

Absolute Coronary Blood Flow Measured by Continuous Thermodilution in Patients With Ischemia and Nonobstructive Disease, J. Am. Coll. Cardiol. 77 (2021) 728–741. https://doi.org/10.1016/j.jacc.2020.12.019.

[33] M. Lodi Rizzini, D. Gallo, G. De Nisco, F. D'Ascenzo, C. Chiastra, P.P. Bocchino, F. Piroli, G.M. De Ferrari, U. Morbiducci, Does the inflow velocity profile influence physiologically relevant flow patterns in computational hemodynamic models of left anterior descending coronary artery?, Med. Eng. Phys. 82 (2020) 58–69. https://doi.org/10.1016/j.medengphy.2020.07.001.

[34] P. Xaplanteris, S. Fournier, D.C.J. Keulards, J. Adjedj, G. Ciccarelli, A. Milkas, M. Pellicano, M. Van't Veer, E. Barbato, N.H.J. Pijls, B. De Bruyne, Catheter-based measurements of absolute coronary blood flow and microvascular resistance feasibility, safety, and reproducibility in humans, Circ. Cardiovasc. Interv. 11 (2018) 1–8. https://doi.org/10.1161/CIRCINTERVENTIONS.117.006194.

[35] C. Chiastra, D. Gallo, P. Tasso, F. Iannaccone, F. Migliavacca, J.J. Wentzel, U. Morbiducci, Healthy and diseased coronary bifurcation geometries influence near-wall and intravascular flow: A computational exploration of the hemodynamic risk, J. Biomech. 58 (2017) 79–88. https://doi.org/10.1016/j.jbiomech.2017.04.016.

[36] J. Busch, D. Giese, L. Wissmann, S. Kozerke, Reconstruction of divergence-free velocity fields from cine 3D phase-contrast flow measurements, Magn. Reson. Med. 69 (2013) 200–210. https://doi.org/10.1002/mrm.24221.

[37] D. Tresoldi, M. Cadioli, R. Ponzini, A. Esposito, F. De Cobelli, U. Morbiducci, G. Rizzo, Mapping aortic hemodynamics using 3D cine phase contrast magnetic resonance parallel imaging: Evaluation of an anisotropic diffusion filter, Magn. Reson. Med. 71 (2014) 1621–1631. https://doi.org/10.1002/mrm.24811.

[38] D. Gallo, D.A. Steinman, P.B. Bijari, U. Morbiducci, Helical flow in carotid bifurcation as surrogate marker of exposure to disturbed shear, J. Biomech. 45 (2012) 2398–2404. https://doi.org/10.1016/j.jbiomech.2012.07.007.

[39] P. Jaccard, The distribution of the flora in the alpine zone, New Phytol. 11 (1912) 37–50. https://doi.org/https://doi.org/10.1111/j.1469-8137.1912.tb05611.x.

[40] G.B. Thurston, Frequency and shear rate dependence of viscoelasticity of human blood., Biorheology. 10 (1973) 375–381. https://doi.org/10.3233/bir-1973-10311.

[41] U. Morbiducci, D. Gallo, D. Massai, R. Ponzini, M.A. Deriu, L. Antiga, A. Redaelli, F.M. Montevecchi, On the importance of blood rheology for bulk flow in hemodynamic models of the carotid bifurcation, J. Biomech. 44 (2011) 2427–2438. https://doi.org/10.1016/j.jbiomech.2011.06.028.

[42] A.M. Malek, S.L. Alper, S. Izumo, Hemodynamic Shear Stress and Its Role in Atherosclerosis, JAMA. 282 (1999) 2035–2042. https://doi.org/10.1001/jama.282.21.2035.

[43] J.J. Wentzel, Y.S. Chatzizis, F.J.H. Gijsen, G.D. Giannoglou, C.L. Feldman, P.H. Stone, Endothelial shear stress in the evolution of coronary atherosclerotic plaque and vascular remodelling: Current understanding and remaining questions, Cardiovasc. Res. 96 (2012) 234–243. https://doi.org/10.1093/cvr/cvs217.

[44] U. Morbiducci, R. Ponzini, M. Grigioni, A. Redaelli, Helical flow as fluid dynamic signature for atherogenesis risk in aortocoronary bypass. A numeric study, J. Biomech. 40 (2007) 519–534. https://doi.org/10.1016/j.jbiomech.2006.02.017.

[45] U. Morbiducci, R. Ponzini, D. Gallo, C. Bignardi, G. Rizzo, Inflow boundary conditions for image-based computational hemodynamics: Impact of idealized versus measured velocity profiles in the human aorta, J. Biomech. 46 (2013) 102–

109. https://doi.org/10.1016/j.jbiomech.2012.10.012.

[46]   D.G. Altman, T.M. Bland, Measurement in Medicine : The Analysis of Method
       Comparison Studies Author (s): D . G . Altman and J . M . Bland Published by :
       Wiley for the Royal Statistical Society Stable URL :
       http://www.jstor.org/stable/2987937 REFERENCES Linked references are ava,
       Statistician. 32 (1983) 307–317.

[47]   A. Kumar, O.Y. Hung, M. Piccinelli, P. Eshtehardi, M.T. Corban, D. Sternheim, B.
       Yang, A. Lefieux, D.S. Molony, E.W. Thompson, W. Zeng, Y. Bouchi, S. Gupta, H.
       Hosseini, M. Raad, Y.A. Ko, C. Liu, M.C. McDaniel, B.D. Gogas, J.S. Douglas, A.A.
       Quyyumi, D.P. Giddens, A. Veneziani, H. Samady, Low Coronary Wall Shear Stress
       Is Associated With Severe Endothelial Dysfunction in Patients With Nonobstructive
       Coronary Artery Disease, JACC Cardiovasc. Interv. 11 (2018) 2072–2080.
       https://doi.org/10.1016/j.jcin.2018.07.004.

[48]   V. Tufaro, H. Safi, R. Torii, B.K. Koo, P. Kitslaar, A. Ramasamy, A. Mathur, D.A.
       Jones, R. Bajaj, E. Erdoğan, A. Lansky, J. Zhang, K. Konstantinou, C.D. Little, R.
       Rakhit, G. V. Karamasis, A. Baumbach, C. V. Bourantas, Wall shear stress
       estimated by 3D-QCA can predict cardiovascular events in lesions with borderline
       negative fractional flow reserve, Atherosclerosis. 322 (2021) 24–30.
       https://doi.org/10.1016/j.atherosclerosis.2021.02.018.

[49]   E. Barbato, W. Aarnoudse, W.R. Aengevaeren, G. Werner, V. Klauss, W. Bojara, I.
       Herzfeld, K.G. Oldroyd, N.H.J. Pijls, B. De Bruyne, Validation of coronary flow
       reserve measurements by thermodilution in clinical practice, (2003).
       https://doi.org/10.1016/j.ehj.2003.11.009.

[50]   H. Everaars, G.A. de Waard, R.S. Driessen, I. Danad, P.M. van de Ven, P.G.

Raijmakers, A.A. Lammertsma, A.C. van Rossum, P. Knaapen, N. van Royen, Doppler Flow Velocity and Thermodilution to Assess Coronary Flow Reserve: A Head-to-Head Comparison With [15O]H2O PET, JACC Cardiovasc. Interv. 11 (2018) 2044–2054. https://doi.org/10.1016/j.jcin.2018.07.011.

[51] J.C.H. Schuurbiers, N.G. Lopez, J. Ligthart, F.J.H. Gijsen, J. Dijkstra, P.W. Serruys, A.F. Van der Steen, J.J. Wentzel, In vivo validation of CAAS QCA-3D coronary reconstruction using fusion of angiography and intravascular ultrasound (ANGUS), Catheter. Cardiovasc. Interv. 73 (2009) 620–626. https://doi.org/10.1002/ccd.21872.

[52] R. Ponzini, M. Lemma, U. Morbiducci, F.M. Montevecchi, A. Redaelli, Doppler derived quantitative flow estimate in coronary artery bypass graft: A computational multiscale model for the evaluation of the current clinical procedure, Med. Eng. Phys. 30 (2008) 809–816. https://doi.org/10.1016/j.medengphy.2007.09.004.

[53] J.T.C. Schrauwen, J.C.V. Schwarz, J.J. Wentzel, A.F.W. Van Der Steen, M. Siebes, F.J.H. Gijsen, The impact of scaled boundary conditions on wall shear stress computations in atherosclerotic human coronary bifurcations, Am. J. Physiol. - Hear. Circ. Physiol. 310 (2016) H1304–H1312. https://doi.org/10.1152/ajpheart.00896.2015.

[54] B. De Bruyne, N.H.J. Pijls, L. Smith, M. Wievegg, G.R. Heyndrickx, Coronary Thermodilution to Assess Flow Reserve, Circulation. 104 (2001) 2003–2006. https://doi.org/10.1161/hc4201.099223.

[55] N.H.J. Pijls, B. De Bruyne, L. Smith, W. Aarnoudse, E. Barbato, J. Bartunek, G.J.W. Bech, F. Van De Vosse, Coronary thermodilution to assess flow reserve: Validation in humans, Circulation. 105 (2002) 2482–2486. https://doi.org/10.1161/01.CIR.0000017199.09457.3D.

[56] A. Manginas, P. Gatzov, C. Chasikidis, V. Voudris, G. Pavlides, D. V. Cokkinos, Estimation of coronary flow reserve using the Thrombolysis In Myocardial Infarction (TIMI) frame count method, Am. J. Cardiol. 83 (1999) 1562–1564. https://doi.org/10.1016/S0002-9149(99)00149-6.

[57] S.K. Chugh, J. Koppel, M. Scott, L. Shewchuk, D. Goodhart, R. Bonan, J.C. Tardif, S.G. Worthley, C. Dimario, M.J. Curtis, I.T. Meredith, T.J. Anderson, Coronary flow velocity reserve does not correlate with TIMI frame count in patients undergoing non-emergency percutaneous coronary intervention, J. Am. Coll. Cardiol. 44 (2004) 778–782. https://doi.org/10.1016/j.jacc.2004.05.048.

[58] D.S. Molony, L.H. Timmins, O.Y. Hung, E. Rasoul-Arzrumly, H. Samady, D.P. Giddens, An assessment of intra-patient variability on observed relationships between wall shear stress and plaque progression in coronary arteries, Biomed. Eng. Online. 14 (2015) S2. https://doi.org/10.1186/1475-925X-14-S1-S2.

[59] E.M.J. Hartman, G. De Nisco, F.J.H. Gijsen, S.A. Korteland, A.F.W. van der Steen, J. Daemen, J.J. Wentzel, The definition of low wall shear stress and its effect on plaque progression estimation in human coronary arteries, Sci. Rep. 11 (2021) 1–11. https://doi.org/10.1038/s41598-021-01232-3.

[60] T.J. Pedley, The Fluid Mechanics of Large Blood Vessels, Cambridge University Press, Cambridge, 1980. https://doi.org/DOI: 10.1017/CBO9780511896996.

[61] D. Zhu, G. Bonanno, A.G. Hays, R.G. Weiss, M. Schär, Phase contrast coronary blood velocity mapping with both high temporal and spatial resolution using triggered Golden Angle rotated Spiral k-t Sparse Parallel imaging (GASSP) with shifted binning, Magn. Reson. Med. 86 (2021) 1929–1943. https://doi.org/10.1002/mrm.28837.